



# Optical, crystallographic and Judd–Ofelt analysis of europium doped $\text{Sr}_6\text{Y}_2\text{Al}_4\text{O}_{15}$ nanocrystals for NUV-WLED fabrication

Hina Dalal<sup>1</sup>, Priyanka Sehrawat<sup>1</sup>, Monika Sheoran<sup>1</sup>, Mukesh Kumar<sup>1</sup>, and R. K. Malik<sup>1,\*</sup>

<sup>1</sup>Department of Chemistry, Maharshi Dayanand University, Rohtak 124001, India

**Received:** 18 August 2021

**Accepted:** 5 November 2021

**Published online:**

19 November 2021

© The Author(s), under exclusive licence to Springer Science+Business Media, LLC, part of Springer Nature 2021

## ABSTRACT

A very convenient and energy-saving route named Solution-Combustion Synthesis had been adopted to prepare a sequence of  $\text{Sr}_6\text{Y}_2\text{Al}_4\text{O}_{15}:\text{Eu}^{3+}$  (1.0–5.0 mol%) nanophosphor having an excellent luminescence which is very requisite in the solid-state illumination sector. The monoclinic phase and the crystallinity of the prepared samples were confirmed by Powder X-Ray Diffraction and the Rietveld refinement technique. Non-uniformity and somewhat agglomeration of particles having a size between 32 nm and 62 nm, were observed during morphological probes via Scanning and Transmission Electron Microscopies. The red-light emission was due to electronic transition from  $^5\text{D}_0 \rightarrow ^7\text{F}_2$  states which is purely electric-dipole allowed transition. Dexter's approach as well as Inokuti-Hirayama model, were cast-off to look into photoluminescent properties. Both these models confirmed the multipolar interactions as the main cause for concentration quenching after 3.0 mol% of Europium(III) content. Various other radiative properties such as decay-time, quantum efficiency, non-radiative relaxation rates were also determined. Red light parameters like Color Coordinate Temperature and Commission International de l'Eclairage color coordinates were also evaluated which confirmed the potential candidature of the prepared nanophosphors for the most recent version of wLEDs, lasers, sensors, advanced solar cells, etc.

## 1 Introduction

A fast-paced increase in the world's population always demands new economical sources of energy production. Energy conservation is also a challenging task. Keeping the world's energy demands and

environmental contamination in mind, it is very necessary to search for new technology to produce green energy and also to tune the existing methods in an eco-friendly manner. The illumination demands can be fulfilled with the use of phosphors because of their significant toxic-free nature. The most

Address correspondence to E-mail: lion.singh0108@gmail.com

prominent use of phosphors is in the new generation SSL (Solid State Lighting) appliances [1]. One common route for wLED fabrication involves the coating of a blue InGaN chip with yttrium aluminum garnet (YAG) doped with  $\text{Ce}^{3+}$  phosphor [2–4]. But this method is not much economical because of its limiting properties such as high CCT, small CRI (Color Rendering Index), etc. [5]. Therefore, it is a great requisite to search for some economical and environment-friendly methods and materials that overweighs the difficulties in the fabrication of wLEDs without harming nature. Rare-earth doped nanophosphors play a major role in this direction because of their highly fascinating properties like good CRI, great luminance in the visible region, high quantum efficiency, and eco-friendly nature [6, 7]. Due to the presence of deeply buried 4f shells, lanthanide ions produce sharp emission peaks in the visible region that make them a powerful source of desired colored light production. For this purpose, the two prime requirements are a suitable host and a good dopant. Therefore, an efficient, less toxic, thermally stable, having broadband-gap and high surface/volume ratio  $\text{Sr}_6\text{Y}_2\text{Al}_4\text{O}_{15}$  has been selected as a host matrix and  $\text{Eu}^{3+}$  ions have been selected as dopant ions due to its attractive optical properties. A collective emission can be obtained from a somewhat yellow to a red region with an increase in the concentration of activator ions due to charge transfer from  $\text{O}^{2-}$  to  $\text{Eu}^{3+}$  ions [8, 9]. No report is available in the literature on the doping of tripositive europium ions on the present host which represents the novelty of the given research in the illumination sector. A very efficient and ecofriendly solution combustion method was used to synthesize the given phosphor [10]. Thereafter, the structural and photophysical attributes were studied in detail with the help of different techniques. A thorough structural analysis was done using X-ray diffraction patterns and the Rietveld refinement platform. Photoluminescent and energy gap studies were done using different types of spectrophotometers. Particle size distribution and surface morphology were depicted with Transmission Electron Microscopy and Scanning Electron Microscopy techniques. Quantum efficiencies and non-radiative rates were also calculated. At last, CIE and CCT values were examined and found in such a place that makes the given nanophosphor very color-tunable for near UV wLEDs fabrication.

## 2 Synthetic procedure and characterizations

A series of monoclinic phased  $\text{Sr}_6\text{Y}_2\text{Al}_4\text{O}_{15}:\text{Eu}^{3+}$  nanophosphor with red emission was generated through a low-cost energy-efficient and eco-friendly solution combustion route. The products obtained by this method were homogeneous and highly crystalline in nature [11]. All the raw constituents were purchased from Sigma Aldrich (Lab and Production Materials) with 99.99% purity such as metal nitrates (acting as oxidizers)  $\text{Y}(\text{NO}_3)_3 \cdot 6\text{H}_2\text{O}$ ,  $\text{Sr}(\text{NO}_3)_2 \cdot 6\text{H}_2\text{O}$ ,  $\text{Al}(\text{NO}_3)_3 \cdot 9\text{H}_2\text{O}$ ,  $\text{Eu}(\text{NO}_3)_3 \cdot 6\text{H}_2\text{O}$  and  $\text{NH}_2\text{CONH}_2$  (urea) used as organic fuel (reducing agent) and were taken in stoichiometric amount with the ratio of fuel and oxidizer 1:1. All elements were dissolved in a little amount of triple distilled water in a pyrex beaker (250 ml). The beaker was set on a hot plate maintained at  $\approx 100^\circ\text{C}$  for 8–10 min to make the solution clear and homogeneous that resulted in a gel-type material further making the combustion process smoother. Then the resulted mixture was laid into a muffle furnace ( $\approx 500^\circ\text{C}$ ) for around 15 min. A self-sustained redox exothermic reaction took place and a voluminous, solid, and crispy powder was obtained. The voluminous nature of the final product can be explained by the evolution of large amounts of gases such as  $\text{CO}_2$ ,  $\text{N}_2$ , and water vapors that make the product porous and crystalline. After that, the product was cooled down to room temperature and finely crushed in an agate mortar. This attained powder was further sintered in a silica crucible at  $1100^\circ\text{C}$  for 3 h to refine the existing properties of the prepared phosphor. The final product formed was again allowed to attain room temperature and mortared to get a fine powdered form and stored in a desiccator for various characterizations.

The crystallinity and purity of phase formed of manufactured nanophosphor were examined with the assistance of PXRD outlines recorded using Bragg–Brentano geometry Rigaku-Ultima IV (Japan) diffractometer working with  $\text{Cu-K}\alpha$  radiation, a detector, and a nickel filter. The machine was operated in such a manner that tube current and voltage were adjusted at 40 mA and 40 kV respectively. The diffraction profile for all nanocrystals was recorded between the range of  $10^\circ$  and  $80^\circ$  with a scanning speed of  $2^\circ$  per minute and  $0.02^\circ$  of scanning step. The crystal structure was further refined via the Rietveld refinement technique with GSAS (General

Structural Analysis System) platform and various refined parameters were calculated [12–14]. The shifted Chebysckew function with 3 terms was operated for background refinement. Also, the Pseudo-Voigt function is being employed to fit the outlines of XRD peaks [15, 16].

Particle shape, size distribution, and topography were inspected with JEOL JSM-6510 (Japan) SEM and TECNAI G<sup>2</sup>FEI TEM instruments. Energy band-gap studies were done via diffuse reflectance spectrum recorded with a Shimadzu UV–Vis 3600 Plus spectrophotometer furnished with a sphere accessory in the 200–800 nm range. Decay curves and photoluminescent aspects were investigated with a Hitachi F-7000 spectrophotometer equipped with Xe light source. Lastly, CIE and CCT coordinates were calculated using the MATLAB program.

### 3 Results and discussion

#### 3.1 Purity of phase

Monoclinic phased crystalline Sr<sub>6</sub>Y<sub>2</sub>Al<sub>4</sub>O<sub>15</sub>:Eu<sup>3+</sup> nanophosphor with ICSD#262993 [17] was precisely investigated by recording powder diffraction patterns (portrayed in Fig. 1a) for all prepared nanophosphors. The observed patterns of the prepared nanophosphor were compared to that of standard host lattice that was found to match with the latter except for small differences. There is some small extra peaks present that may arise due to some extra phase formed in the given host lattice. To overcome these small differences, Rietveld refinement over the optimized sample (displayed in Fig. 1b) was done using shifted Chebysckew function with 3 terms. Monoclinic crystal system with C121 space group and cell parameters  $a = 17.669 \text{ \AA}$ ,  $b = 5.767 \text{ \AA}$ ,  $c = 7.699 \text{ \AA}$ ,  $\alpha = \gamma = 90^\circ$  and  $\beta = 90.879^\circ$ , the convergence of refined parameters occurred at  $R_p = 9.70\%$ ,  $wR_p = 13.90\%$  and reduced  $\chi^2 = 3.955$ . A comparison between crystallographic data of host and doped optimized sample was also done that is summarized in Table 1. In the doped samples, the Sr<sup>2+</sup> or Al<sup>3+</sup> or Y<sup>3+</sup> ions can be replaced with that of dopant ions (Eu<sup>3+</sup>). But the charge and size difference between Sr<sup>2+</sup> and Eu<sup>3+</sup> ions and size difference between Al<sup>3+</sup> and Eu<sup>3+</sup> ions ruled out their replacement by the latter. Therefore, the only possible ions that can bear the replacement by the dopant cations

are Y<sup>3+</sup> ions due to almost similar size to that of the latter. This replacement can further be confirmed by calculating the percentage ionic difference ( $\Delta_r$ ) that should be less than 30% for ideal substitution [18–20]. The following equation can be used to calculate the same:

$$\Delta_r = \frac{R_m(\text{CN}) - R_d(\text{CN})}{R_m(\text{CN})} \times 100 \quad (1)$$

Here,  $R_m(\text{CN})$  and  $R_d(\text{CN})$  represent the effective ionic radii of host and doped cations respectively in which CN stands for coordination number. The value of the parameter  $\Delta_r$  for Al<sup>3+</sup> and Y<sup>3+</sup> ions were found 79.24% and 5.55% respectively. Since  $\Delta_r$  value for Y<sup>3+</sup> ions found to be less than 30% which confirms their replacement with the doped cations. The crystal structure of optimized nanophosphor Sr<sub>6</sub>Y<sub>1.94</sub>Eu<sub>0.06</sub>Al<sub>4</sub>O<sub>15</sub> was retrieved from Diamond: Crystal Impact Software system that is depicted in Fig. 1c along with coordination polyhedra of four types of Sr<sup>2+</sup> atoms present labeled as Sr1, Sr2, Sr3, and Sr4 with coordination numbers 9, 9, 8 and 8 respectively. Also, the observed bond distances and interatomic constraints are summarized in Tables 2 and 3.

Moreover, the average size of manufactured crystals was determined using XRD data via Scherrer's equation [21] as follows:

$$D = \frac{0.941\lambda}{\beta \cos\theta} \quad (2)$$

At this point,  $d$  stands for mean crystallite size in nm,  $\theta$  is the diffraction angle,  $\lambda$  denotes the wavelength of X-ray used (0.15406 nm) and  $\beta$  denotes FWHM (Full Width at Half Maxima) in radians. Using all the above values, 'd' was found out to be in the range between 32 nm and 62 nm which almost coincides with the average size calculated experimentally using TEM analysis. Also, the mean crystallite size increases with an increase in dopant concentration (shown in Fig. 1d) which can be explained with the phenomenon 'agglomeration'.

#### 3.2 Morphological and elemental analysis

Morphological probes such as particle size, shape, and nature of the prepared nanophosphor were performed via SEM and TEM analysis, which revealed an irregular shape with porous nature. These pores and voids present in phosphor confirmed the solution combustion synthetic route due

**Fig. 1 a** Combined PXRD patterns of  $\text{Sr}_6\text{Y}_{2(1-x)}\text{Al}_4\text{O}_{15}:\text{xEu}^{3+}$  ( $x = 1.0\text{--}5.0$  mol%) nanophosphor. **b** Rietveld refinement over optimized nanophosphor  $\text{Sr}_6\text{Y}_{1.94}\text{Eu}_{0.06}\text{Al}_4\text{O}_{15}$  yielding refined parameters of  $W_{\text{Rp}} = 13.90\%$ ,  $R_{\text{p}} = 9.70\%$  and  $\chi^2 = 3.955$ . **c** Overall crystal structure of the optimized sample  $\text{Sr}_6\text{Y}_{1.94}\text{Eu}_{0.06}\text{Al}_4\text{O}_{15}$  along with coordination spheres of various types of Sr atoms present. **d** Variation of crystallite size with dopant concentration for  $\text{Sr}_6\text{Y}_2\text{Al}_4\text{O}_{15}:\text{Eu}^{3+}$  (1.0–5.0 mol%) nanophosphor

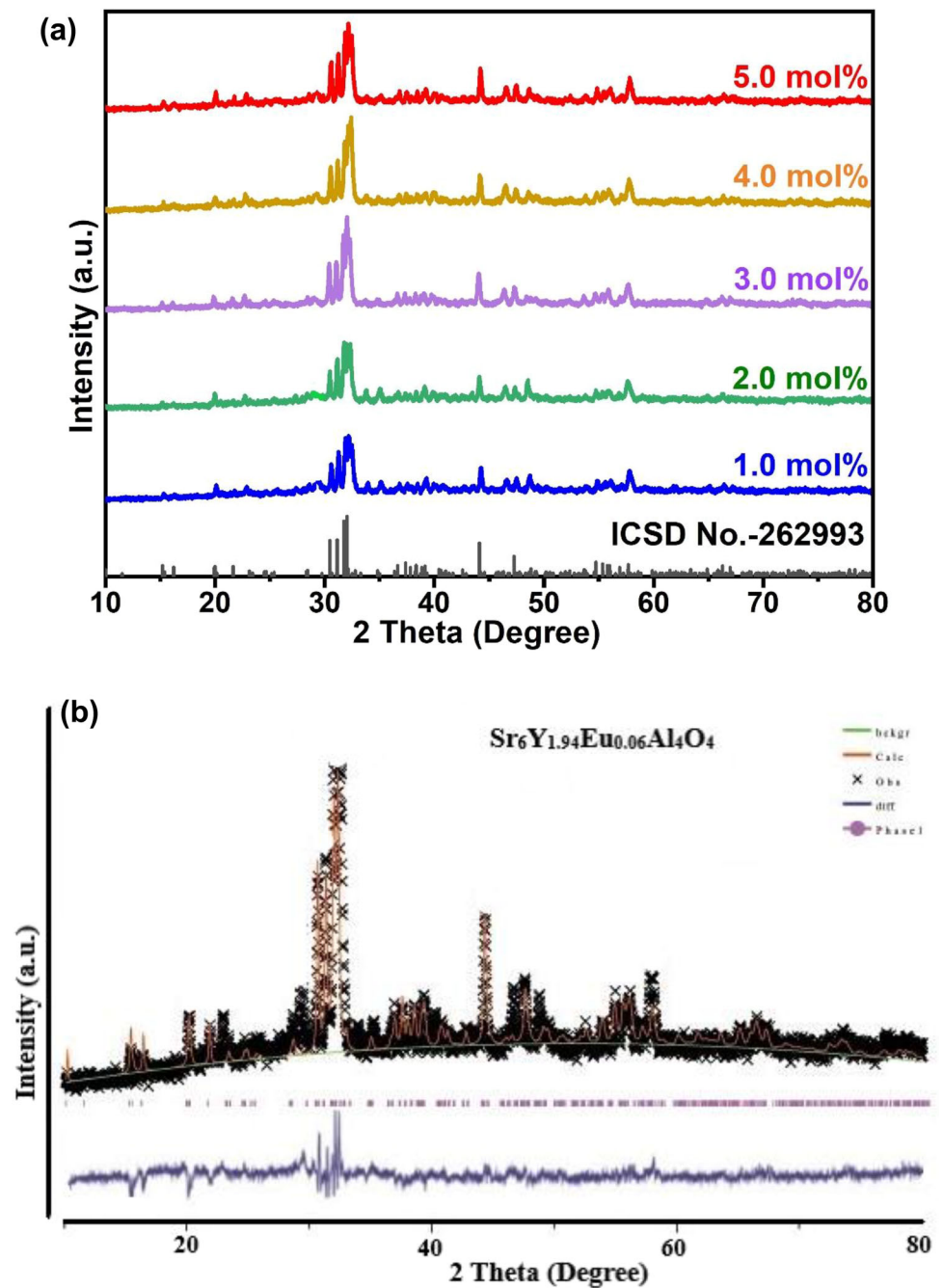
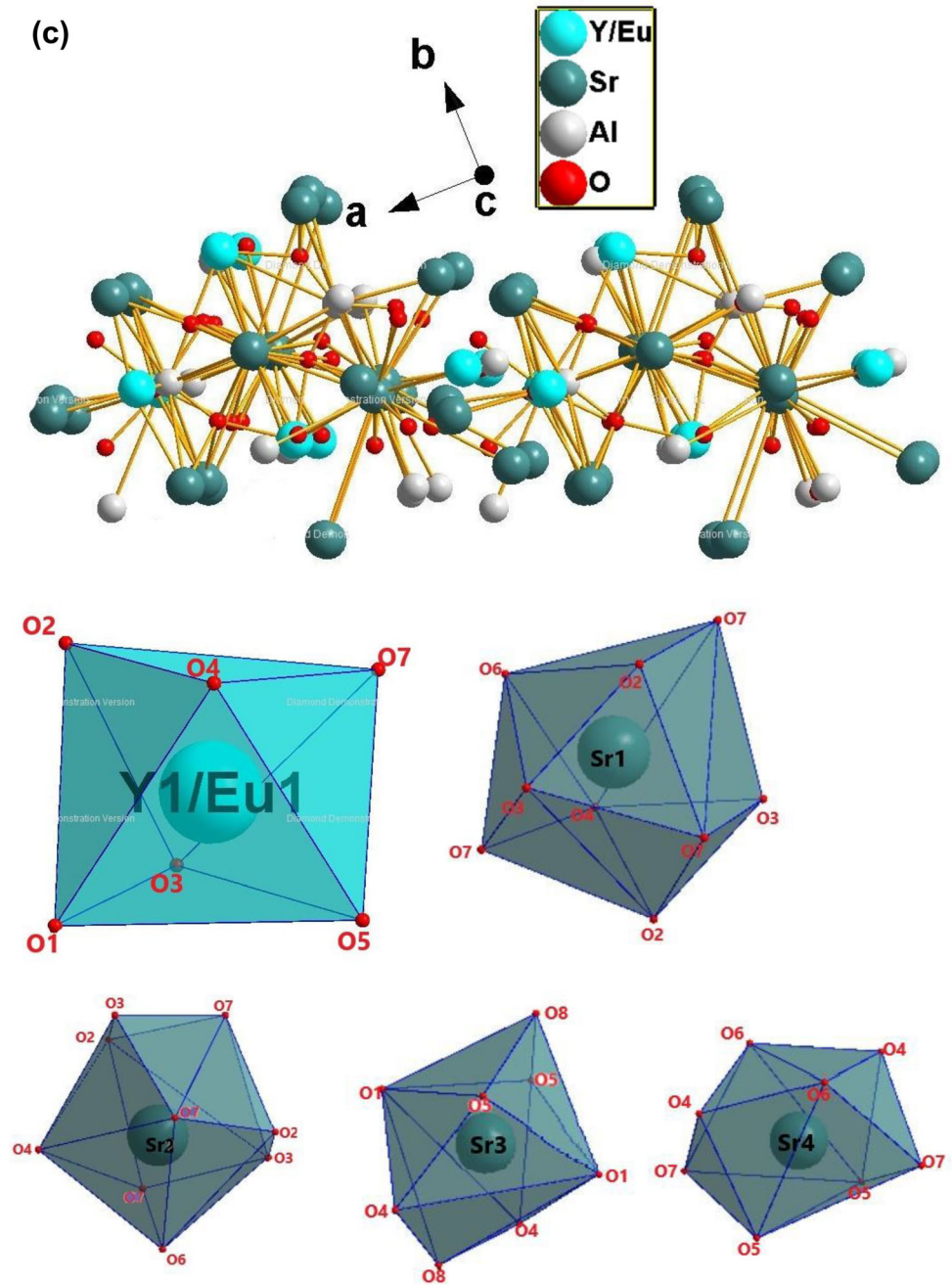




Fig. 1 continued



to escaping of numerous gases [22, 23]. Figure 2a and b reports the SEM micrograph of as-synthesized (500 °C) and sintered (1100 °C) nanophosphor whilst the Fig. 2c and d represents the TEM and SAED (Selected Area Electron Diffraction) patterns of the optimized nanophosphor respectively. The concentric fringes present in the SAED patterns unveiled the polycrystalline nature of the prepared phosphors. For qualitative and quantitative elemental analysis of the prepared sample, EDAX (Energy Dispersive X-Ray

Analysis) platform was taken into use. Figure 2e and f represent the EDS spectrum of host and doped matrix respectively describing the relative number of various elements present in a particular selected field of view. EDS mapping was also performed for the doped optimized sample which revealed the presence of all elements quantitatively. The only presence of elements Sr, Y, Al, O, and Eu in EDS mapping of optimized nanophosphor (Fig. 2g) sharply indicates

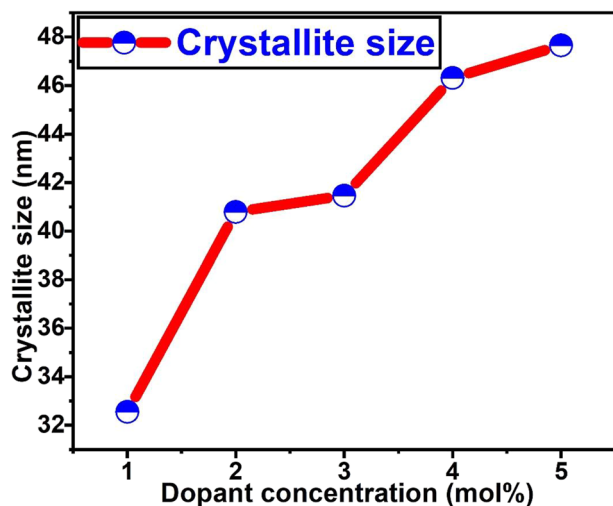


Fig. 1 continued

**Table 1** A comparison of different crystal parameters of optimized nanophosphor  $\text{Sr}_6\text{Y}_{1.94}\text{Eu}_{0.06}\text{Al}_4\text{O}_{15}$  with pure host  $\text{Sr}_6\text{Y}_2\text{Al}_4\text{O}_{15}$

Formula	$\text{Sr}_6\text{Y}_2\text{Al}_4\text{O}_{15}$	$\text{Sr}_6\text{Y}_{1.94}\text{Eu}_{0.06}\text{Al}_4\text{O}_{15}$
Formula Weight ( $\text{g mol}^{-1}$ )	1051.45	1055.23
Symmetry	Monoclinic	Monoclinic
Space group	C121(5)	C121(5)
a ( $\text{\AA}$ )	17.6039(5)	17.669(31)
b ( $\text{\AA}$ )	5.7455(2)	5.767(10)
c ( $\text{\AA}$ )	7.6733(2)	7.699(13)
Z	2	2
$\alpha = \gamma$ (degree)	90	90
$\beta$ (degree)	90.794(26)	90.879(19)
Volume of cell ( $\text{\AA}^3$ )	776.03(3)	784.41(400)
Density ( $\text{g cm}^{-3}$ )	4.499	4.4674
Pearson code	mc54	mc54
Wyckoff sequence	c12ba2	c12ba2

the efficient doping of  $\text{Eu}^{3+}$  ions in the given sample without involving any impurity atoms [24].

### 3.3 Optical analysis and mechanism of energy transfer

The photoluminescent excitation bands of complete  $\text{Sr}_6\text{Y}_{2(1-x)}\text{Eu}_{2x}\text{Al}_4\text{O}_{15}$  ( $x = 0.01\text{--}0.05$ ) nanocrystal series are precisely displayed in Fig. 3a in the range 320–420 nm recorded at 613 nm. A broad band absorption occurred in this wavelength range which corresponds to the host absorption. A somewhat

broader band in the lower wavelength side centered at 328 nm appears due to charge transfer from filled 2p-orbital of  $\text{O}^{2-}$  to empty 4f-orbital of  $\text{Eu}^{3+}$  ions [25]. Apart from charge transfer spectra, many intra-configurational f-f transitions also took place with varying intensities. A rather weaker intensity band occurred at 364 nm due to  ${}^7\text{F}_0 \rightarrow {}^5\text{D}_4$  transition. Two stronger bands appeared at 386 and 396 nm arising from  ${}^7\text{F}_0 \rightarrow {}^5\text{G}_2$  and  ${}^7\text{F}_0 \rightarrow {}^5\text{L}_6$  electronic transitions, respectively out of which the transition occurring at 396 nm is the most intense at which the emission spectra were recorded. The combined 3-D emission spectra depicted in Fig. 3b show various emission peaks in the wavelength range 510–710 nm with different intensities. The relative intensities of different emission peaks are also collected in Table 4. From Fig. 3b, it can be perceived that the intensity of the most intense transition progressively decreases after reaching a certain amount of dopant concentration (in this case 3.0 mol%) which is shown as a supplementary figure in Fig. 3b. The most intense peak appearing at 613 nm arises from  ${}^5\text{D}_0 \rightarrow {}^7\text{F}_2$  pure electric-dipole allowable transition ( $\Delta_J = \pm 1$ ) [26]. This transition is solely responsible for the red color of manufactured nanophosphor. Another high-intensity peak observed at 582 nm is pure magnetic-dipole allowed transition for which ( $\Delta_J = 0, \pm 1$ ) [27] occurring in the states  ${}^5\text{D}_0$  to  ${}^7\text{F}_1$ . Both these transitions are characteristic transitions of  $\text{Eu}^{3+}$  ions [3, 28]. Also, four other lower intensity transitions arise from  ${}^5\text{D}_2 \rightarrow {}^7\text{F}_3$  (526 nm),  ${}^5\text{D}_0 \rightarrow {}^7\text{F}_0$  (568 nm),  ${}^5\text{D}_0 \rightarrow {}^7\text{F}_3$  (663 nm) and  ${}^5\text{D}_0 \rightarrow {}^7\text{F}_4$  (690 nm) electronic states. A decline in the photoluminescent intensity was also observed after a certain concentration known as optimum concentration (in this case 3.0 mol%). This decrease in PL intensity after the optimized concentration (3.0 mol%) of the dopant ions can be explained due to the phenomenon of non-radiative relaxation. After reaching a certain concentration of  $\text{Eu}^{3+}$  ions, the rate of non-radiative relaxation exceeds that of radiative relaxation which finally descends the PL emission intensity. All these excitation-emission, charge transfer, radiative and non-radiative processes can more be clarified with an elaborate energy level map (depicted in Fig. 3c). In the phenomenon of a decrease in PL intensity after 3.0 mol% of activator ions, critical distance plays an important role which is calculated via the following formulation given by Blasse [29, 30]:

**Table 2** Refined atomic parameters and occupancies of various elements present in BaY<sub>0.95</sub>Tb<sub>0.05</sub>Zn<sub>3</sub>AlO<sub>7</sub> nanophosphor

Atom	Ion type	Wyck	Occupancy	x/a	y/b	z/c	U (Å <sup>2</sup> )
Y1	Y <sup>3+</sup>	4c	0.97	0.3442	0.4886	0.7532	0.0003
Sr1	Sr <sup>2+</sup>	4c	1.00	0.1753	0.4801	0.0.5062	0.0003
Sr2	Sr <sup>2+</sup>	4c	1.00	0.1606	0.4669	0.9687	0.0003
Sr3	Sr <sup>2+</sup>	2a	1.00	0.0000	0.0387	0.0000	0.0003
Sr4	Sr <sup>2+</sup>	2b	1.00	0.0000	0.0985	0.5000	0.0003
Al1	Al <sup>3+</sup>	4c	1.00	0.3110	0.4786	0.2445	0.0003
Al2	Al <sup>3+</sup>	4c	1.00	0.0119	0.5318	0.2262	0.0003
O1	O <sup>2-</sup>	4c	1.00	0.3627	0.4931	0.0497	0.0003
O2	O <sup>2-</sup>	4c	1.00	0.2591	0.2144	0.2340	0.0003
O3	O <sup>2-</sup>	4c	1.00	0.2422	0.7066	0.2297	0.0003
O4	O <sup>2-</sup>	4c	1.00	0.0886	0.3316	0.2607	0.0003
O5	O <sup>2-</sup>	4c	1.00	0.0400	0.8196	0.2705	0.0003
O6	O <sup>2-</sup>	4c	1.00	0.9280	0.4122	0.3051	0.0003
O7	O <sup>2-</sup>	4c	1.00	0.3426	0.4869	0.4630	0.0003
O8	O <sup>2-</sup>	2a	1.00	0.0000	0.5232	0.0000	0.0003
Eu1	Eu <sup>3+</sup>	4c	0.03	0.3442	0.4886	0.7532	0.0003

**Table 3** Certain interatomic distances (Å) in the crystal structure of Sr<sub>6</sub>Y<sub>1.94</sub>Eu<sub>0.06</sub>Al<sub>4</sub>O<sub>15</sub> nanophosphor system

Bond type	Distance (Å)	Bond type	Distance(Å)
Y1/Eu1-O7	2.2339(38) × 1	Sr3-O1	2.4761(42) × 1
Y1/Eu1-O3	2.2354(27) × 1	Sr3-O1	2.4763(42) × 1
Y1/Eu1-O2	2.2451(29) × 1	Sr3-O5	2.5273(31) × 1
Y1/Eu1-O5	2.2770(33) × 1	Sr3-O5	2.5277(31) × 1
Y1/Eu1-O1	2.3011(38) × 1	Sr3-O8	2.7940(48) × 1
Y1/Eu1-O4	2.3104(31) × 1	Sr3-O8	2.9730(52) × 1
Sr1-O6	2.3822(29) × 1	Sr3-O4	3.0391(31) × 1
Sr1-O4	2.5617(29) × 1	Sr3-O4	3.0393(31) × 1
Sr1-O2	2.6645(29) × 1	Sr4-O5	2.4992(28) × 1
Sr1-O3	2.7772(31) × 1	Sr4-O5	2.4996(28) × 1
Sr1-O7	2.8722(49) × 1	Sr4-O6	2.6614(28) × 1
Sr1-O3	2.9425(31) × 1	Sr4-O6	2.6616(28) × 1
Sr1-O7	2.9494(50) × 1	Sr4-O4	2.7823(29) × 1
Sr1-O7	2.9800(52) × 1	Sr4-O4	2.7826(29) × 1
Sr1-O2	3.0045(31) × 1	Sr4-O7	2.8647(47) × 1
Sr2-O2	2.5605(26) × 1	Al1-O7	1.7654(27) × 1
Sr2-O6	2.6251(33) × 1	Al1-O1	1.7699(23) × 1
Sr2-O4	2.7139(34) × 1	Al1-O2	1.7792(24) × 1
Sr2-O3	2.7601(28) × 1	Al1-O3	1.7930(22) × 1
Sr2-O1	2.7663(47) × 1	Al1-O6	3.2733(40) × 1
Sr2-O3	2.8175(30) × 1	Al2-O8	1.7518(29) × 1
Sr2-O8	2.8696(49) × 1	Al2-O3	1.7525(23) × 1
Sr2-O2	3.0352(31) × 1	Al2-O6	1.7639(27) × 1
Sr2-O1	3.0654(52) × 1	Al2-O5	1.7979(22) × 1

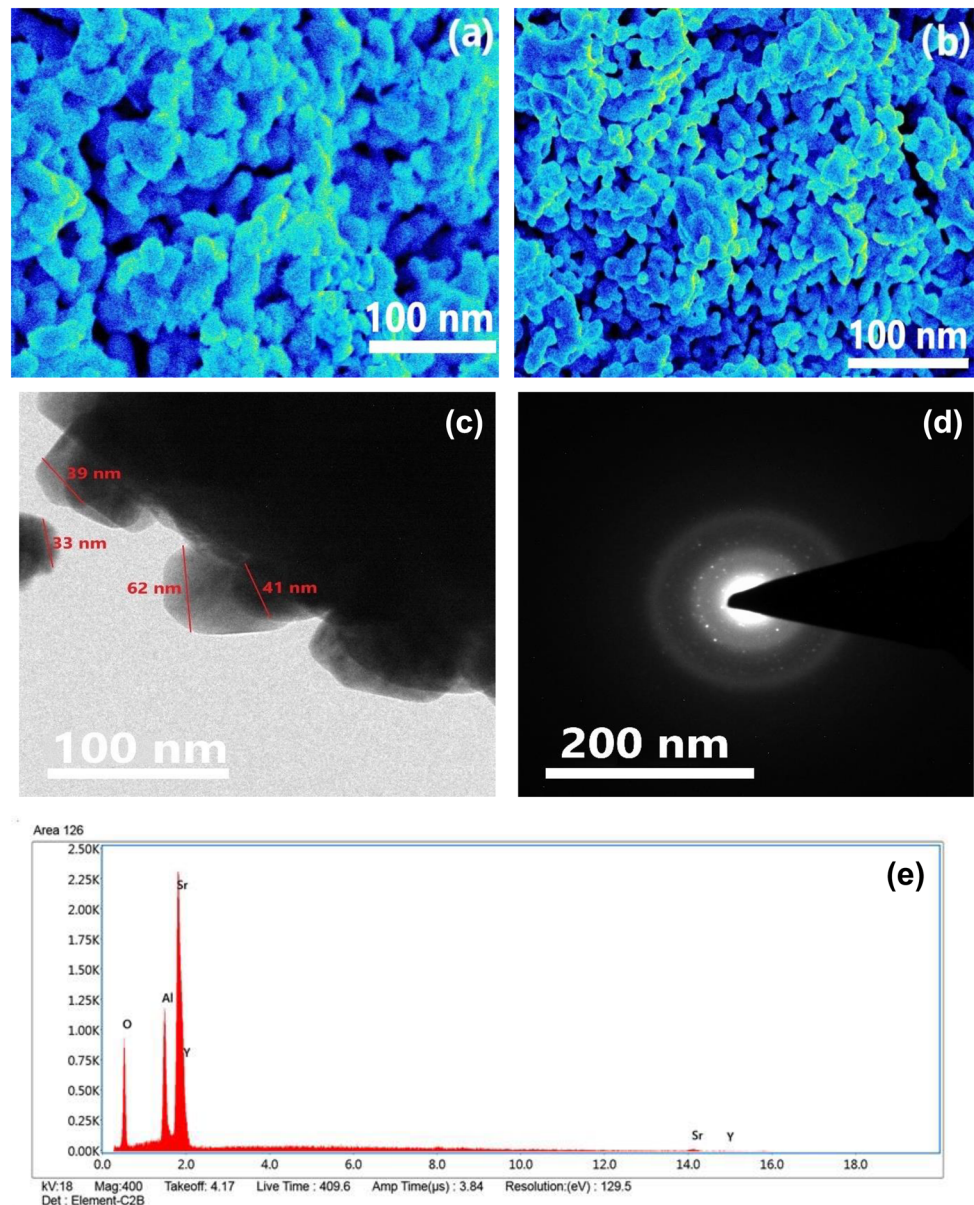
$$R_c = 2 \left[ \frac{3V}{4\pi x_c N} \right]^{1/3} \tag{3}$$

Here, N denotes the number of replaceable cations in one unit cell, V and x<sub>c</sub> are used for volume of one unit cell and optimal concentration of dopant ions respectively. In the present case, x<sub>c</sub> = 0.03, V = 784.41 Å<sup>3</sup>, and N = 2, critical distance is found to be 14.61 Å that is plenty higher than the acceptable value of R<sub>c</sub> = 5 Å for the energy exchange process to take place. Consequently, the exchange process cannot be the reason for energy migration. As there was no overlapping found in the excitation and emission spectra of the prepared nanophosphor, radiative reabsorption is also ruled out. Hence, multipolar interactions must be responsible for such phenomenon which is further explained by Dexter’s theory as follows [31]:

$$\log \left( \frac{I}{C} \right) = - \frac{s}{d} \log(C) + \log(f) \tag{4}$$

In this formulation, I/C stands for the ratio between PL emission intensity and Eu<sup>3+</sup> concentration, f is any constant, and s signifies different values for different types of inter-linkages that cause concentration quenching. A plot of log(I/C) vs log(C) produces a slope of 1.1315 (represented in Fig. 3d) that produces s value to be 3.3945 (≈ 3) thus evidencing the multipolar interactions accountable for the concentration quenching mechanism. This mechanism was also certified with the help of I-H model generalization stating that during the process of non-radiative relaxation direct energy relocation (DET) and migration-assisted energy relocation

**Fig. 2** SEM micrographs of **a** As synthesized (500 °C) and **b** Optimized nanophosphor sintered at 1100 °C. **c** and **d** respectively represents TEM AND SAED patterns of  $\text{Sr}_6\text{Y}_{1.94}\text{Eu}_{0.06}\text{Al}_4\text{O}_{15}$  nanophosphor. **e** EDS spectrum of host matrix  $\text{Sr}_6\text{Y}_2\text{Al}_4\text{O}_{15}$ . **f** EDS spectrum of optimized doped nanophosphor  $\text{Sr}_6\text{Y}_{1.94}\text{Eu}_{0.06}\text{Al}_4\text{O}_{15}$ . **g** Energy Dispersive Maps of all elements present in optimized doped nanophosphor  $\text{Sr}_6\text{Y}_{1.94}\text{Eu}_{0.06}\text{Al}_4\text{O}_{15}$



(MAET), two phenomena come into existence. For the given nanopowders, DET amongst adjacent  $\text{Eu}^{3+}$  ions is dominant that can be confirmed from decay-data [32].

$$I(t) = I_0 \exp \left\{ -\frac{t}{\tau_0} - Q \left( \frac{t}{\tau_0} \right)^s \right\} \quad (5)$$

In this formulation,  $\tau_0$ ,  $t$  and  $Q$  stand for decay time of donor ions without the presence of acceptor ions, decay time, and energy relocation constraint respectively, so that [33]

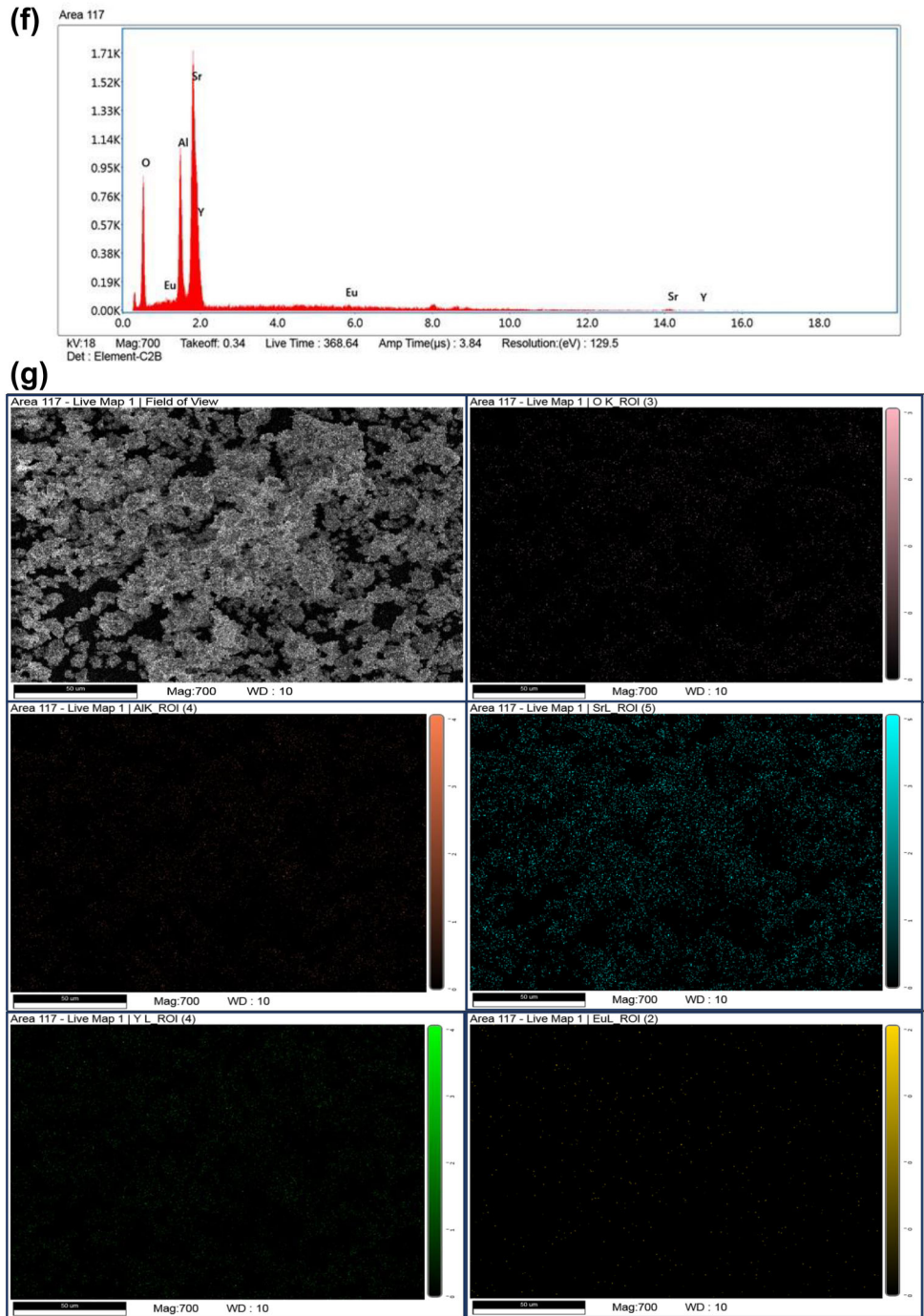
$$Q = \frac{4\pi}{3} \tau \left( 1 - \frac{3}{s} \right) N_0 R_0^3 \quad (6)$$

Here  $N_0$  stands for dopant composition and  $R_0$  signifies critical distance. The I-H plot is best fitted with  $s = 3$  (reported in Fig. 3e) which validates the multipolar interactions as the main cause for quenching mechanism and the value of  $\tau$  was found to be 3.1863.

Also, the rates of non-radiative transitions (collected in Table 5) for all prepared nanophosphors can be calculated using the following formulation:



Fig. 2 continued



$$\frac{1}{\tau_0} = \frac{1}{\tau_R} + A_{nR} \tag{7}$$

where  $\tau_0$  and  $\tau_R$  are the observed and radiative lifetimes respectively.  $\tau_0$  values for all phosphors are collected in Table 5 showing a decreasing trend in lifetime values (portrayed in Fig. 3f) and  $\tau_R$  was calculated by using Auzel's method [34, 35] as follows:

$$\tau(c) = \frac{\tau_R}{1 + \frac{c}{c_0} e^{-N/3}} \tag{8}$$

Here,  $\tau(c)$  is the decay lifetime at concentration 'c', N is the phonon number, and  $c_0$  is the concentration constant. From this equation (Auzel's fitting in Origin Software) the value of  $\tau_R$  was found to be 2.27 ms.

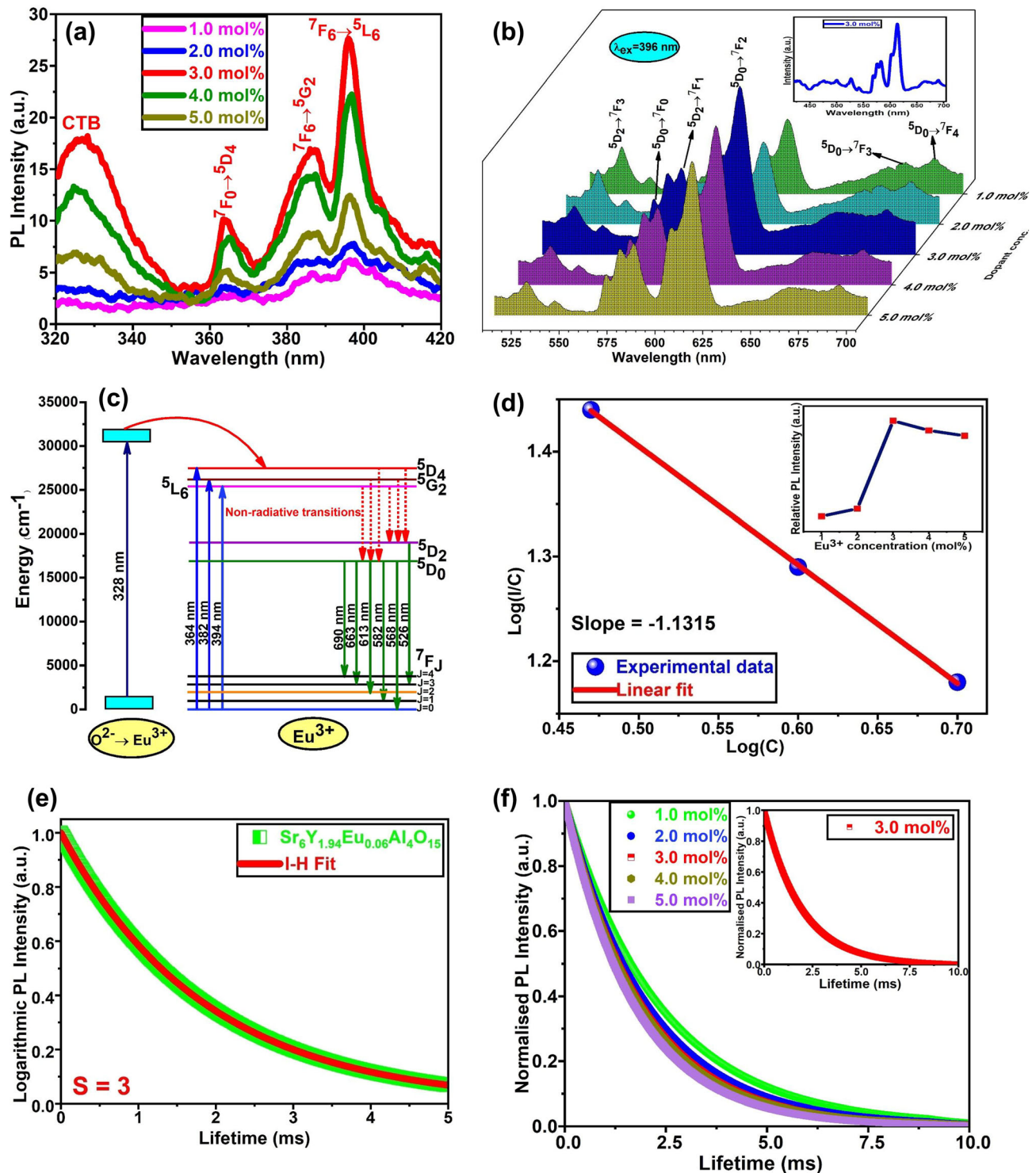


**Fig. 3** **a** Combined PL excitation spectra of  $\text{Sr}_6\text{Y}_{2(1-x)}\text{Al}_4\text{O}_{15}:x\text{Eu}^{3+}$  ( $x = 1.0$ – $5.0$  mol%) nanophosphor recorded at  $\lambda_{\text{em}} = 613 \text{ nm}$ . **b** Combined 3-D PL emission spectra of  $\text{Sr}_6\text{Y}_{2(1-x)}\text{Al}_4\text{O}_{15}:x\text{Eu}^{3+}$  ( $x = 1.0$ – $5.0$  mol%) nanophosphor recorded at  $\lambda_{\text{ex}} = 396 \text{ nm}$ . **c** A descriptive energy level diagram showing different electronic transitions in different energy levels. **d** A linear

plot between  $\text{Log}(I/C)$  and  $\text{Log}(C)$  with inset showing variation of PL intensity with increase in concentration of dopant ions in  $\text{Sr}_6\text{Y}_{2(1-x)}\text{Al}_4\text{O}_{15}:x\text{Eu}^{3+}$  ( $x = 1.0$ – $5.0$  mol%) nanophosphor. **e** I-H model fit graph resulting in a value of  $S = 3$ . **f** Lifetime decay curves of  $\text{Sr}_6\text{Y}_{2(1-x)}\text{Al}_4\text{O}_{15}:x\text{Eu}^{3+}$  ( $x = 1.0$ – $5.0$  mol%) nanophosphor recorded at  $\lambda_{\text{ex}} = 396 \text{ nm}$  and  $\lambda_{\text{em}} = 613 \text{ nm}$

**Table 4** Different electronic transitions taking place in the spectrum of Sr<sub>6</sub>Y<sub>2(1-x)</sub>Eu<sub>2x</sub>Al<sub>4</sub>O<sub>15</sub> (x = 1–5 mol %) nanophosphors along with their intensity and position

Nanophosphor	Kind of spectrum	Transitions	Wave number (cm <sup>-1</sup> )	Intensity
Sr <sub>6</sub> Y <sub>2(1-x)</sub> Eu <sub>2x</sub> Al <sub>4</sub> O <sub>15</sub>	Excitation at λ <sub>em</sub> = 613 nm Emission at λ <sub>ex</sub> = 396 nm	O <sup>2-</sup> → Eu <sup>3+</sup>	30,488	Strong
		<sup>7</sup> F <sub>0</sub> → <sup>5</sup> D <sub>4</sub>	27,473	Medium
		<sup>7</sup> F <sub>6</sub> → <sup>5</sup> G <sub>2</sub>	25,907	Strong
		<sup>7</sup> F <sub>6</sub> → <sup>5</sup> L <sub>6</sub>	25,253	Very strong
		<sup>5</sup> D <sub>2</sub> → <sup>7</sup> F <sub>3</sub>	19,011	Weak
		<sup>5</sup> D <sub>0</sub> → <sup>7</sup> F <sub>0</sub>	17,605	Weak
		<sup>5</sup> D <sub>0</sub> → <sup>7</sup> F <sub>1</sub>	17,182	Strong
		<sup>5</sup> D <sub>0</sub> → <sup>7</sup> F <sub>2</sub>	16,313	Very strong
		<sup>5</sup> D <sub>0</sub> → <sup>7</sup> F <sub>3</sub>	15,083	Very weak
		<sup>5</sup> D <sub>0</sub> → <sup>7</sup> F <sub>4</sub>	14,493	Very weak

**Table 5** Photoluminescence decay lifetime, quantum efficiency and non-radiative rates for Sr<sub>6</sub>Y<sub>2(1-x)</sub>Eu<sub>2x</sub>Al<sub>4</sub>O<sub>15</sub> (1–5 mol%) nanophosphors

Eu <sup>3+</sup> concentration (mol%)	Lifetime (ms)	Quantum efficiency (%)	Non-radiative rates (s <sup>-1</sup> )
1	2.12	93	31.1
2	1.85	81	100.0
3	1.70	75	147.7
4	1.67	73	158.3
5	1.56	69	200.5

Further, the quantum efficiency is simply the ratio of observed and radiative lifetime values;

$$\varphi = \frac{\tau_0}{\tau_R} \tag{9}$$

The quantum efficiency decreases with an increase in activator ions concentration because the observed lifetime decreases due to non-radiative energy transfer among activator ions [36] and is found to be 75% for the optimized sample.

### 3.4 Band-gap Examination and study of Thermal Stability

Energy band-gap (E<sub>g</sub>) for pure host Sr<sub>6</sub>Y<sub>2</sub>Al<sub>4</sub>O<sub>15</sub> as well as optimized nanophosphor Sr<sub>6</sub>Y<sub>1.94</sub>Eu<sub>0.06</sub>Al<sub>4</sub>O<sub>15</sub> were evaluated via Kubelka–Munk formulation [37] giving a plot between photon energy and absorption coefficient (α) [Fig. 4a and b respectively] with corresponding DR spectrum in the insets. The general equation for E<sub>g</sub> based on DR spectrum is:

$$[F(R_\infty)hv]^n = C(hv - E_g) \tag{10}$$

Here, hv signifies the energy of a photon, C is a constant of proportionality and E<sub>g</sub> is the band-gap. The value of n = 0.5, 1.5, 2, and 3 are taken for indirect-allowed, direct forbidden, direct allowed and indirect forbidden electronic transitions respectively.

The Kubelka–Munk Theory expresses the value of F(R<sub>∞</sub>) through the following formulation [38]:

$$F(R_\infty) = \frac{(1 - R_\infty)^2}{2R_\infty} = \frac{K}{S} \tag{11}$$

Here, S is the scattering coefficient and K denotes absorption coefficient. R<sub>∞</sub> stands for R<sub>sample</sub>/R<sub>standard</sub>. The extrapolated line to F(R<sub>∞</sub>)hv = 0 yields a value of band-gap of 5.02 eV for the host matrix and 3.46 eV for the optimized doped sample (3.0 mol%). The lower value of the band-gap of the doped sample is less than that of the pure host makes the prepared nanophosphor very suitable for wLEDs fabrication.

Furthermore, the thermal stability of the optimized nanosample (Sr<sub>6</sub>Y<sub>1.94</sub>Eu<sub>0.06</sub>Al<sub>4</sub>O<sub>15</sub>) was studied by its thermogravimetric analysis (TGA) performed by a Perkin Elmer STA 6000 thermogravimeter. The resulted thermogram is represented in Fig. 4c, which illustrates a little weight-loss below 235 °C due to evaporation of the water molecules absorbed on the surface of the prepared nanosample. Also, the combustion of nitrates present in the fabricated nanophosphor decreases the weight of the sample occurs up to 900 °C such that no weight loss takes place beyond this temperature, thus indicating the thermal stability of the prepared nanomaterial.

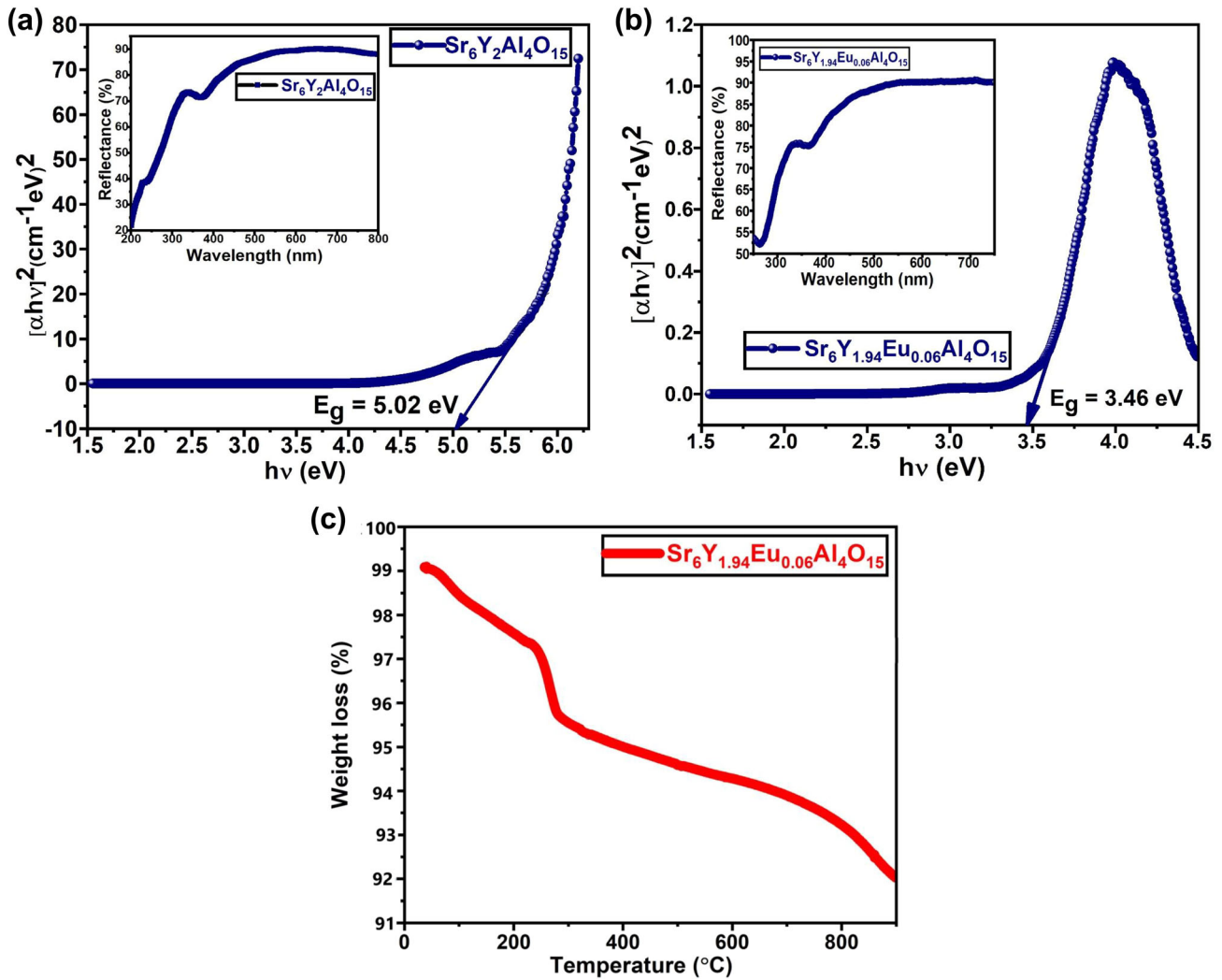


**Fig. 4** a Tauc's plot to calculate band-gap ( $E_g$ ) for host matrix  $\text{Sr}_6\text{Y}_2\text{Al}_4\text{O}_{15}$ . b Tauc's plot to calculate band-gap ( $E_g$ ) for optimized nanophosphor  $\text{Sr}_6\text{Y}_{1.94}\text{Eu}_{0.06}\text{Al}_4\text{O}_{15}$ . c TGA (Thermo

Gravimetric Analysis) curve for optimized nanophosphor  $\text{Sr}_6\text{Y}_{1.94}\text{Eu}_{0.06}\text{Al}_4\text{O}_{15}$  recorded upto 900 °C

### 3.5 Judd–Ofelt parameterization

Photoluminescent emanation spectra of  $\text{Eu}^{3+}$  doped nanophosphors were utilized to calculate J–O intensity parameters. The transition  ${}^5\text{D}_0 \rightarrow {}^7\text{F}_1$  comes under the magnetically allowed transition category while the transitions  ${}^5\text{D}_0 \rightarrow {}^7\text{F}_J$  ( $J = 2, 4, 6$ ) are electric-dipole allowed transitions. Host matrix affects the intensity of electric dipole allowed transitions while the magnetically allowed transitions are completely host independent. The J–O parameters ( $\Omega_2$ ,  $\Omega_4$ , and  $\Omega_6$ ) have been found by using the ratio between the intensity of two electronic transitions  ${}^5\text{D}_0 \rightarrow {}^7\text{F}_J$  ( $J = 2, 4, 6$ ) and  ${}^5\text{D}_0 \rightarrow {}^7\text{F}_1$  using the following expression:

$$\frac{f_{I_J} dv}{f_{I_1} dv} = \frac{A_J}{A_1} = \frac{e^2 v_J^3 n(n^2 + 2)^2}{S_{MD} v_1^3 9n^3} \Omega_\lambda \left| \langle \psi_J || U^\lambda || \psi_1' \rangle \right|^2 \quad (12)$$

Here,  $v_1$  and  $v_J$  stand for wavenumbers corresponding to  ${}^5\text{D}_0 \rightarrow {}^7\text{F}_J$  ( $J = 2, 4, 6$ ) and  ${}^5\text{D}_0 \rightarrow {}^7\text{F}_1$  electronic transitions.  $S_{MD}$  denotes line strength of magnetically allowed transition  ${}^5\text{D}_0 \rightarrow {}^7\text{F}_1$ .

In the present samples, as the  ${}^5\text{D}_0 \rightarrow {}^7\text{F}_6$  transitions are missing, therefore,  $\Omega_6$  parameter can be neglected. The value of the other two intensity parameters  $\Omega_2$  and  $\Omega_4$  and their ratio for all nanophosphors (1.0–5.0 mol%) are collected in Table 6.  $\Omega_2$  and  $\Omega_4$  are related to short-range and long-range characteristics of host lattice respectively [39]. A typically high value



**Table 6** Judd–Ofelt parameters ( $\Omega_2$  and  $\Omega_4$ ) and their corresponding ratio of  $\text{Sr}_6\text{Y}_{2(1-x)}\text{Eu}_{2x}\text{Al}_4\text{O}_{15}$  ( $x = 0.01\text{--}0.05$  mol%)

$\text{Sr}_6\text{Y}_{2(1-x)}\text{Eu}_{2x}\text{Al}_4\text{O}_{15}$ (mol%)	$\Omega_2$ ( $\times 10^{-20}$ cm <sup>-2</sup> )	$\Omega_4$ ( $\times 10^{-20}$ cm <sup>-2</sup> )	$\Omega_2/\Omega_4$
1	7.77	0.98	7.92
2	7.76	0.97	8.00
3	10.75	0.36	29.86
4	10.58	0.35	30.22
5	10.43	0.39	26.74

**Table 7** Color chromaticity and CCT coordinates along with CCT values of  $\text{Sr}_6\text{Y}_{2(1-x)}\text{Eu}_{2x}\text{Al}_4\text{O}_{15}$  (1.0–5.0 mol%) nanophosphor samples

$\text{Sr}_6\text{Y}_{2(1-x)}\text{Eu}_{2x}\text{Al}_4\text{O}_{15}$ (mol%)	CIE coordinates (x, y)	(u', v')	CCT (K)
1	0.3636, 0.3458	0.2264, 0.4845	4299
2	0.3583, 0.3470	0.2222, 0.4843	4489
3	0.4128, 0.3513	0.2584, 0.4947	2972
4	0.4035, 0.3515	0.2517, 0.4934	3187
5	0.4303, 0.3516	0.2706, 0.4976	2620

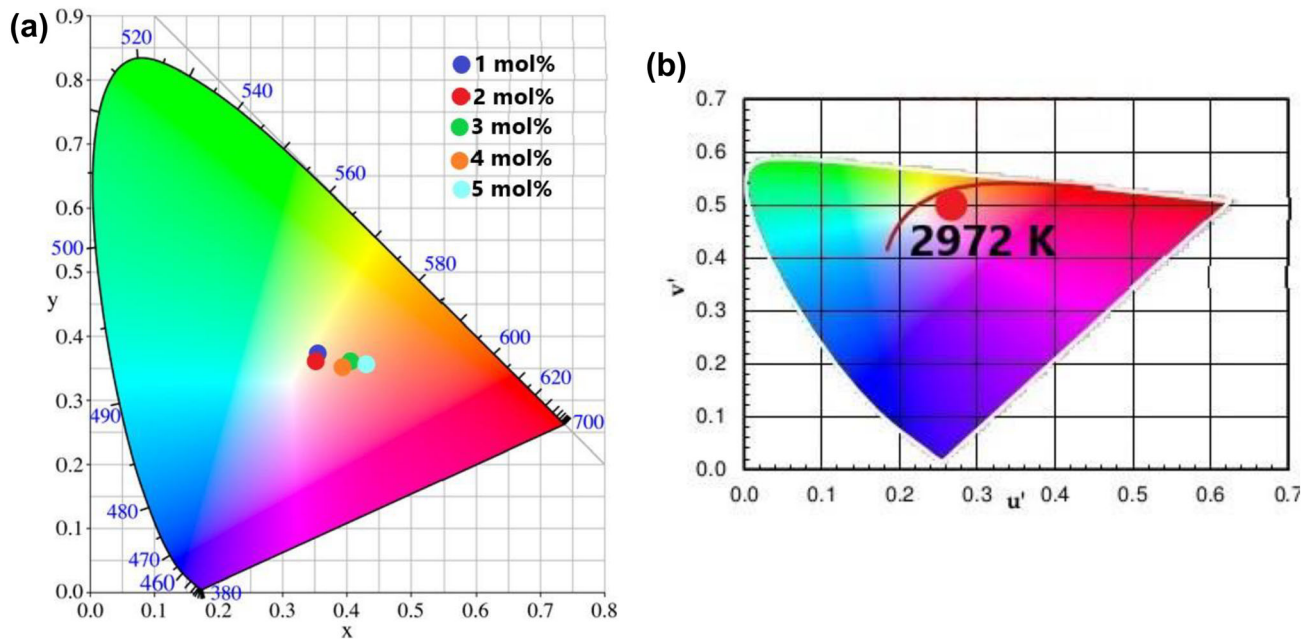


**Fig. 5** **a** CIE chromaticity diagram of  $\text{Sr}_6\text{Y}_{2(1-x)}\text{Al}_4\text{O}_{15}:\text{xEu}^{3+}$  ( $x = 1.0\text{--}5.0$  mol%) nanophosphor. **b** CCT coordinates (u' and v') along with CCT value of optimized nanophosphor  $\text{Sr}_6\text{Y}_{1.94}\text{Eu}_{0.06}\text{Al}_4\text{O}_{15}$

of  $\Omega_2/\Omega_4 = 29.86$  for  $\text{Sr}_6\text{Y}_{1.94}\text{Eu}_{0.06}\text{Al}_4\text{O}_{15}$  nanophosphor confirms the presence of less symmetric surroundings around activator ions ( $\text{Eu}^{3+}$ ) in the crystal lattice which enhances the illuminating properties and makes the prepared nanophosphor more suitable in lighting applications.

### 3.6 CIE color coordinates evaluation

CIE chromaticity diagram graphically represents the colors in a two-dimensional form calculated via MATLAB program using PL emission spectra. The coordinates found for all prepared nanophosphors (1.0–5.0 mol%) are tabulated in Table 7 and displayed in Fig. 5a. All the coordinates calculated are lying in the red section of the CIE chromaticity diagram.

Another CIE parameter, CCT can also be calculated using the following Mc-Camy equation [40]:

$$\text{CCT} = -437n^3 + 3601n^2 - 6861n + 5514.31 \quad (13)$$

Here 'n' denotes the ratio between  $(x-x_e)$  and  $(y-y_e)$  where  $x$  and  $y$  stand for the calculated CIE color coordinates and  $x_e$  and  $y_e$  are the epicenter coordinates (0.332 and 0.186) respectively. Now, the 'u' and 'v' coordinates for CCT can be calculated as follows:

$$u' = \frac{4x}{-2x + 12y + 3} \quad (14)$$

$$v' = \frac{9y}{-2x + 12y + 3} \quad (15)$$

All the calculated values of CCT with respective coordinates  $(u', v')$  are summarized in Table 7. The CCT value calculated for  $\text{Sr}_6\text{Y}_{1.94}\text{Eu}_{0.06}\text{Al}_4\text{O}_{15}$  nanocrystalline nanophosphor was found to be 2972 K (represented in Fig. 5b) that indicates a warm red emission which makes the prepared nanophosphor a strong contender for wLEDs fabrication.

## 4 Conclusions

Red emanating  $\text{Sr}_6\text{Y}_2\text{Al}_4\text{O}_{15}:\text{Eu}^{3+}$  nanocrystalline powder was synthesized via a urea-aided solution-combustion route. The crystallinity and monoclinic phase with space group C121 were confirmed with Rietveld refinement over X-ray diffraction data. Non-uniform nature with some agglomeration of particles with size in the range between 32 nm and 48 nm was observed during morphological investigations through SEM and TEM techniques. The red-light emanation was manifested by an electronic transition at 613 nm with an excitation wavelength of 395 nm. Maximum lumen output was observed with 3.0 mol% of europium concentration after which the phenomenon of concentration quenching was detected that arises from dipole–dipole types of interactions. The decay time, quantum efficiency, and non-radiative rates were found to be 1.70 ms, 75%, and  $147.7 \text{ s}^{-1}$  respectively for the optimized sample. CIE and CCT coordinates were also calculated that were found to lie in the red region of the chromaticity diagram making the nanocrystalline powder a suitable contender for WLEDs, digital communication, sensors, lasers, and advanced solar cells.

## Acknowledgements

Hina Dalal, gratefully thanks University Grants Commission (UGC) for providing monetary aid in form of JRF with award no. (49/(CSIRNETJUNE2019)).

## Declarations

**Conflict of interest** The authors have no conflicts of interest for declaration.

## References

1. V.R. Bandi, B.K. Grandhe, K. Jang, H.-S. Lee, D.-S. Shin, S.-S. Yi, J.-H. Jeong, J. Alloys Compd. **512**, 264 (2012)
2. F. Baur, F. Glocker, T. Jüstel, J. Mater. Chem. C **3**, 2054 (2015)
3. P. Sehrawat, R.K. Malik, N. Kumari, M. Punia, S.P. Khatkar, V.B. Taxak, Chem. Phys. Lett. **770**, 138438 (2021)
4. P. Sehrawat, S.P. Khatkar, I.J. Kim, R.K. Malik, P. Chhillar, V.B. Taxak, Chem. Phys. Lett. **762**, 138134 (2020)
5. G.K. Behrh, R. Gautier, C. Latouche, S. Jobic, H. Serier-Brault, Inorg. Chem. **55**, 9144 (2016)
6. P. Sehrawat, R.K. Malik, S.P. Khatkar, V.B. Taxak, Chem. Phys. Lett. **773**, 138592 (2021)
7. P. Sehrawat, R.K. Malik, R. Punia, M. Sheoran, N. Kumari, S.P. Khatkar, V.B. Taxak, J Mater Sci: Mater Electron **32**, 15930 (2021)
8. H. Hafez, M. Saif, M.S.A. Abdel-Mottaleb, J. Power Sources **196**, 5792 (2011)
9. L. Liu, S.K. Gill, Y. Gao, L.J. Hope-weeks, K.H. Cheng, Forensic. Sci. Int. **176**, 163 (2008)
10. P. Sehrawat, R.K. Malik, R. Punia, S.P. Khatkar, V.B. Taxak, Chem. Phys. Lett. **777**, 138743 (2021)
11. P. Sehrawat, R.K. Malik, R. Punia, S.P. Khatkar, V.B. Taxak, J. Alloys Compd. **879**, 160371 (2021)
12. P. Sehrawat, R.K. Malik, M. Sheoran, R. Punia, Chem. Phys. Lett. **777**, 138752 (2021)
13. M. Sheoran, P. Sehrawat, M. Kumar, N. Kumari, V.B. Taxak, S.P. Khatkar, R.K. Malik, Optik **241**, 167041 (2021)
14. M. Sheoran, P. Sehrawat, M. Kumar, N. Kumari, V.B. Taxak, S.P. Khatkar, R.K. Malik, J. Mater. Sci. Mater. Electron. **32**, 11683 (2021)
15. P. Sehrawat, A. Khatkar, P. Boora, M. Kumar, R.K. Malik, S.P. Khatkar, V.B. Taxak, Ceram. Int. **46**, 16274 (2020)
16. G. Li, C.C. Lin, W.T. Chen, M.S. Molokeev, V.V. Atuchin, C.Y. Chiang, W. Zhou, C.W. Wang, W.H. Li, H.S. Sheu, T.S. Chan, C. Ma, R.S. Liu, Chem. Mater. **26**, 2991 (2014)
17. Y. Kawano, S.W. Kim, T. Ishigaki, K. Uematsu, K. Toda, H. Takaba, M. Sato, Opt. Mater. Express **4**, 1770 (2014)

18. R. Venkatesh, N. Dhananjaya, M.K. Sateesh, J.P. Shabaaz Begum, S.R. Yashodha, H. Nagabhushana, C. Shivakumara, *J. Alloys Compd.* **732**, 725 (2018)
19. P. Sehrawat, R.K. Malik, R. Punia, N. Kumari, *Chem. Phys. Lett.* **779**, 138831 (2021)
20. P. Sehrawat, R.K. Malik, R. Punia, M. Sheoran, S. Singh, M. Kumar, *Chem. Phys. Lett.* **781**, 138985 (2021)
21. P. Sehrawat, R.K. Malik, R. Punia, S. Maken, *J Mater Sci: Mater Electron* **32**, 23486 (2021)
22. M.S. Mendhe, S.P. Puppalar, S.J. Dhoble, *Optik* **166**, 15 (2018)
23. Z. Pan, H. Yu, H. Cong, H. Zhang, J. Wang, Q. Wang, Z. Wei, Z. Zhang, R.I. Boughton, *Appl. Optic.* **51**, 7144 (2012)
24. P. Sehrawat, R.K. Malik, R. Punia, M. Sheoran, M. Kumar, S. Maken, *Chem. Phys. Lett.* **758**, 137937 (2020)
25. P. Niu, X. Liu, Y. Wang, W. Zhao, *J. Mater. Sci.: Mater. Electron.* **29**, 124 (2017)
26. S. Das, A. Amarnath Reddy, S. Ahmad, R. Nagarajan, G. Vijaya Prakash, *Chem. Phys. Lett.* **508**, 117 (2011)
27. J.T. Ingle, R.P. Sonekar, S.K. Omanwar, Y. Wang, L. Zhao, *J. Alloys Compd.* **608**, 235 (2014)
28. J. Zhao, C. Guo, T. Li, D. Song, X. Su, *Phys. Chem. Chem. Phys.* **17**, 26330 (2015)
29. G. Blasse, *Phys. Lett.* **28**, 444 (1968)
30. P. Sehrawat, R.K. Malik, R. Punia, M. Sheoran, H. Dalal, *J. Electron. Mater.* **50**, 6964 (2021)
31. J. Xue, M. Song, H.M. Noh, S.H. Park, B.R. Lee, J.H. Kim, J.H. Jeong, *J. Alloys Compd.* **817**, 152705 (2020)
32. Ravina, Naveen, Sheetal, V. Kumar, S. Dahiya, N. Deopa, R. Punia, A.S. Rao, *J. Lumin.* **229**, 117651(2021).
33. T. Manohar, S.C. Prashantha, R. Naik, H. Nagabhushana, H.P. Nagaswarupa, K.S. Anantharaju, K.M. Girish, H.B. Premkumar, *Sensor. Actuator. B Chem.* **243**, 1057 (2017)
34. P. Sehrawat, A. Khatkar, S. Devi, R. Kumar, R.K. Malik, S.P. Khatkar, V.B. Taxak, *Mater. Res. Express.* **6**, 126213 (2019)
35. F. Auzel, *J. Lumin.* **100**, 125 (2002)
36. P. Sehrawat, Dayawati, P. Boora, M. Kumar, R.K. Malik, S.P. Khatkar, V.B. Taxak, *Chem. Phys. Lett.* **759**, 138044 (2020)
37. D. Deng, H. Yu, Y. Li, Y. Hua, G. Jia, S. Zhao, H. Wang, L. Huang, Y. Li, C. Li, S. Xu, *J. Mater. Chem. C* **1** (2013).
38. P. Kubelka, *J. Opt. Soc. Am.* **38**, 448 (1948)
39. P. Sehrawat, A. Khatkar, S. Devi, A. Hooda, S. Singh, R.K. Malik, S.P. Khatkar, V.B. Taxak, *Chem. Phys. Lett.* **737**, 136842 (2020)
40. S. McCamy, *Color Res. Appl.* **17**, 142 (1992)

**Publisher's Note** Springer Nature remains neutral with regard to jurisdictional claims in published maps and institutional affiliations.